

Simulation of site and topographic effects on ground motion in Los Alamos, NM mesas

Swetha Veeraraghavan, Justin L Coleman, Jacobo Bielak

March 2020



The INL is a U.S. Department of Energy National Laboratory operated by Battelle Energy Alliance

Simulation of site and topographic effects on ground motion in Los Alamos, NM mesas

Swetha Veeraraghavan, Justin L Coleman, Jacobo Bielak

March 2020

**Idaho National Laboratory
Idaho Falls, Idaho 83415**

<http://www.inl.gov>

**Prepared for the
U.S. Department of Energy
National Nuclear Security Administration, National Nuclear Security Administration
Under DOE Idaho Operations Office
Contract DE-AC07-05ID14517, DE-AC07-05ID14517**



Simulation of site and topographic effects on ground motion in Los Alamos, NM mesas

Journal:	<i>Geophysical Journal International</i>
Manuscript ID	GJI-18-1122.R1
Manuscript Type:	Research Paper
Date Submitted by the Author:	n/a
Complete List of Authors:	Veeraraghavan, Swetha; Idaho National Laboratory, Coleman, Justin; Idaho National Laboratory, Bielak, Jacobo; Carnegie Mellon University,
Keywords:	North America < GEOGRAPHIC LOCATION, Site effects < SEISMOLOGY, Wave propagation < SEISMOLOGY, Wave scattering and diffraction < SEISMOLOGY, Coda waves < SEISMOLOGY, Earthquake ground motions < SEISMOLOGY

1 submitted to *Geophys. J. Int.*

2
3
4
5
6
7 **Simulation of site and topographic effects on ground motion**
8
9 **in Los Alamos, NM mesas**
10

11
12
13
14 Swetha Veeraraghavan^{1*}, Justin L. Coleman², and Jacobo Bielak³
15

16 ¹ *Idaho National Laboratory, Idaho Falls, ID, USA. Email: swetha.veeraraghavan@inl.gov*

17 ² *Idaho National Laboratory, Idaho Falls, ID, USA. Email: justin.coleman@inl.gov*

18 ³ *Department of Civil and Environmental Engineering, Carnegie Mellon University, Pittsburgh,*
19 *PA, USA. Email: jbielak@cmu.edu*
20
21
22
23
24
25

26 **Abbreviated title:** *Topographic effects in Los Alamos mesas*
27
28

29
30 4 6 July 2019
31
32

33 **SUMMARY**
34

35 Mesas, which consist of an elevated area of land with a flat top and steep cliffs at the sides,
36 are one of the common geological formations present in the Los Alamos region. Previous
37 research has shown that geological formations such as sedimentary canyons can amplify
38 soil response during earthquakes. There have also been parametric studies to understand
39 the response of an idealized and isolated mountain/canyon under inclined plane waves. In
40 this study, a 2D linear anelastic soil domain, with topography modeled after the Los Alamos
41 region with many mesas and canyons, is considered to understand site-specific topographic
42 effects in the presence of non-isolated topographical features. Various earthquake sources
43 configurations ranging from point sources to finite faults with varying rupture length, dip
44 angles, and spatial slip distributions are considered. To isolate the effect of topography,
45 three other soil domains - a homogeneous halfspace, homogeneous halfspace with mesas
46 and canyons, and a computational domain with just the soil properties from the Los Alamos
47 region on a flat soil domain is also considered. 2D site-response analyses of these soil do-
48 mains under earthquake excitation show that the free-field response of the soil can be ampli-
49
50
51
52
53
54
55
56
57
58
59
60

1
2
3 20 fied or deamplified depending on the topography of the region and the location of the station
4
5 21 relative to the fault. These studies also show that even relatively small mesas with height
6
7 22 less than 100 m can significantly amplify the response (by a factor of 2 or more), which
8
9 23 differ from the much smaller amplification factors (≤ 1.2) specified by standard building
10
11 24 codes such as Eurocode-8 (2000) for topographical features with a similar slope. Deam-
12
13 25 plifications are also fairly common, especially close to the canyons. The results from this
14
15 26 study agree qualitatively with those from the ambient vibration study conducted by Stolte
16
17 27 et al. (2017) on a mesa from the Los Alamos region. Thus, such site-specific studies pro-
18
19 28 vide important insights into the variability of the topographic amplification factors within
20
21 29 a region of interest. Such knowledge is important in the design of safety-related critical
22
23 30 infrastructure located within that region.

24 31 **Key words:** Wave propagation, coda waves, north america, earthquake ground motions,
25
26 32 site effects, wave scattering and diffraction

33 1 INTRODUCTION

34 Earthquake waves are generated when slipping occurs between or within plates in the earth's
35
36 35 crust at dislocations or faults. During a fault rupture, energy is released in space and time along
37
38 36 the fault, causing waves to travel outward in all directions. By the time these waves reach the
39
40 37 earth's surface, they might be quite different in both amplitude and frequency content from the
41
42 38 original wave near the fault. This is because the ground motion at a site on the earth's surface
43
44 39 depends not only on the source characteristics, but also on the path the waves follow to the
45
46 40 site, and on local site effects. The path effects arise from rock and soil layers between the fault
47
48 41 and the region of interest, which can amplify or deamplify the wave amplitudes and modify the
49
50 42 frequency content, due to wave dispersion and material damping. Site-specific effects are from
51
52 43 local features such as mountains, canyons, local soil stratigraphy or other geological features
53
54 44 that may lead to additional wave scattering near the site.

55
56 45 The amplification of ground motion due to variation in soil layering has been studied ex-
57
58 46 tensively both experimentally and numerically (e.g., [Stewart et al. \(2008\)](#)). The effects of site-

59
60 * Corresponding author, Email: swetha.veeraraghavan@inl.gov

1
2
3 47 specific characteristics, in specific topography such as in the presence of canyons or hills, have
4
5 48 been observed in many earthquake recordings (Davis & West (1973); Celebi (1987); Spudich
6
7 49 et al. (1996); Caserta et al. (2000); Stewart & Sholtis (2005); Graizer (2009); Marzorati et al.
8
9 50 (2011)) as well as in laboratory tests (Anooshehpour & Brune (1989)). The amplification and
10
11 51 deamplification in the presence of a surface irregularity are due to the constructive and de-
12
13 52 structutive interference, respectively, of the waves. This wave interference has also been numer-
14
15 53 ically demonstrated through parametric studies on idealized shapes of mountains and canyons
16
17 54 subjected to inclined body waves. These numerical studies show that ground motion ampli-
18
19 55 fies on the top of mountains or mesas and there is smaller amplification or deamplification in
20
21 56 canyons (Bouchon (1973); Bard (1982); Sanchez-Sesma et al. (1982); Ashford & Sitar (1997);
22
23 57 Moczo et al. (1997); Poursartip et al. (2017)). Geli et al. (1988) compared numerical results
24
25 58 with earthquake recordings and found that the numerical simulations qualitatively agreed with
26
27 59 the observed results but that the simulations with mathematical models underestimated the
28
29 60 actual amplification. They attributed the quantitative differences to approximations and simpli-
30
31 61 fications used in numerical analyses, mainly simplified topography, homogeneous halfspace,
32
33 62 and absence of neighboring features. To address these issues, efforts have been made in the
34
35 63 recent years to create more detailed 2D and 3D models of select sites with topography and
36
37 64 velocity variations, and to analyze their response under multiple earthquake fault rupture simu-
38
39 65 lations (e.g., Paolucci (2002), Lee et al. (2009), Lovati et al. (2011), Assimaki & Jeong (2013),
40
41 66 Maufroy et al. (2016), and Restrepo et al. (2016)). These studies demonstrate the importance of
42
43 67 site-specific studies to obtain more accurate numerical estimates at sites with complex topog-
44
45 68 raphy.

47
48 69 In a recent study on topographic effects in the alpine regions of Switzerland by Imperatori
49
50 70 & Mai (2015), they analyzed the response of three topographically different zones from this
51
52 71 region under seismic waves generated from point sources. They demonstrated that the pres-
53
54 72 ence of topography causes backscattering of waves towards the source in all three cases, and
55
56 73 that the addition of near-surface low-velocity layers significantly affects the ground response in
57
58 74 the presence of topography. In this study, they also explored the similarities and differences be-
59
60 75 tween the wave scattering that is caused by fine-scale soil heterogeneities (discussed in detail in

1
2
3
4 76 [Imperatori & Mai \(2013\)](#)) to that caused by surface topographical features. While both surface
5
6 77 topography and soil heterogeneities cause significant scattering of seismic waves, they found
7
8 78 that topography causes backscattering of waves as opposed to forward scattering of waves
9
10 79 caused by soil velocity heterogeneities, and this also leads to differences in the time at which
11
12 80 the peak ground motion occurs in these scenarios.

13
14 81 In this study, we focus on the Los Alamos area to understand topographic effects due to
15
16 82 the presence of mesas, i.e., small land formations with relatively flat tops and steep walls,
17
18 83 near the Los Alamos National Laboratory (LANL). [Wong et al. \(2007\)](#) conducted detailed
19
20 84 site characterization to account for shear wave velocity variations near this site; previously,
21
22 85 only simplistic 2D analysis of the LANL sites had been conducted by [Wong et al. \(1995\)](#),
23
24 86 [Silva \(2005\)](#), and [Costantino & Houston \(2005\)](#) to understand the effect of topography. These
25
26 87 studies suggest that the amplification at the top of mesas is less than 20% (i.e., amplification
27
28 88 factor smaller than 1.2) because most of the slopes in these regions are gentle (around 17°).
29
30 89 The 2D studies performed at this site used only plane inclined SH and SV waves as input; these
31
32 90 may not be sufficiently representative of waves that originate from an earthquake fault rupture.
33
34 91 The limited 2D deterministic analyses combined with results from other numerical studies on
35
36 92 idealized and/or isolated topographic features subjected to inclined SV and SH waves ([Paolucci](#)
37
38 93 [\(2002\)](#); [Ashford & Sitar \(1997\)](#); [Pedersen et al. \(1994\)](#); [Geli et al. \(1988\)](#); [Bouchon \(1973\)](#)) and
39
40 94 recommendations from [Eurocode-8 \(2000\)](#) were used to obtain the topographic amplification
41
42 95 factors for the LANL region.

43
44 96 In this paper, the response of a representative 12 km x 10 km 2D cross-section of the LANL
45
46 97 region from the Frijoles canyon to the Rendija canyon [Fig. 1(b)] is simulated to ground mo-
47
48 98 tions from different earthquake sources, ranging from a single point source to finite earthquake
49
50 99 faults with varying dip angles. In order to examine the topographic effects due to the presence
51
52 100 of the mesas, we examine four different settings - flat-homogeneous halfspace (H), mesas and
53
54 101 canyons on top of the homogeneous halfspace (T), horizontally layered system without any
55
56 102 topographical features or flat-layered halfspace(HL), and finally, horizontally layered system
57
58 103 with mesas and canyons (TL). These four systems are analyzed under all the rupture scenarios
59
60 104 to gain physical insight into the effects of site response and topography due to different types

1
2
3 105 of seismic waves. We also qualitatively compare the results from these numerical simulation
4
5 106 with those obtained from recordings of ambient vibration in and around an instrumented ridge
6
7 107 in Mortandad Canyon in the Los Alamos testing area (Stolte et al. (2017)).
8

9 108 It is noteworthy that while the ground motion from 2D simulations differs from actual 3D
10
11 109 ground motion, such 2D simulations are known to capture many of the important features of
12
13 110 ground motion. In this study, we focus on 2D simulations because we are interested in mod-
14
15 111 eling frequencies of engineering interest, up to 10 Hz. Nowadays it is possible to perform 3D
16
17 112 deterministic simulations up to such high frequencies; they are, however, extremely expensive
18
19 113 computationally. Thus, as a first step, it is useful to examine the effects of the mesas on ground
20
21 114 motion using simplified 2D models.
22
23
24

25 115 **2 MODEL DEVELOPMENT**

26 116 **2.1 LANL area stratigraphy - Material model**

27
28 117 Los Alamos is located on the Pajarito plateau, which spans from the Sierra De Los Valles in
29
30 118 the northwest to the Rio Grande river to the southeast [Fig. 1(a)]. Eruptions from the Valles
31
32 119 Caldera volcano in ~ 1.2 Ma and 1.6 Ma is said to have created this plateau (Griggs (1964)).
33
34 120 Therefore, this area mostly contains Bandelier tuff, which is rock composed of volcanic ash.
35
36 121 The depth of these tuffs decreases radially away from the Caldera giving the Pajarito plateau a
37
38 122 gentle slope with higher elevation at the northwest end than at its southeastern end. Many of the
39
40 123 east-trending tributaries of the Rio Grande have eroded parts of the plateau creating the mesas
41
42 124 and canyons in this region. The technical facilities of LANL are located on top of these mesas.
43
44
45
46

47 125 The 2D cross-section considered for this study runs from Frijoles canyon in the south
48
49 126 (35.7893° - 106.2593°) to Rendija canyon in the north (35.9099° , - 106.2593°) cutting through
50
51 127 many mesas and canyons [Fig. 1(b)]. As the northern end is closer to the Caldera than the
52
53 128 southern end, the elevations at the northern end are slightly higher than at the southern end.
54
55 129 The variation in elevation along the 2D cross-section is presented in Fig. 2. This elevation as a
56
57 130 function of distance is obtained from the United States geological survey (USGS) 1 m digital
58
59 131 elevation map for this region. While elevation data is available every at 1 m, elevation data at
60

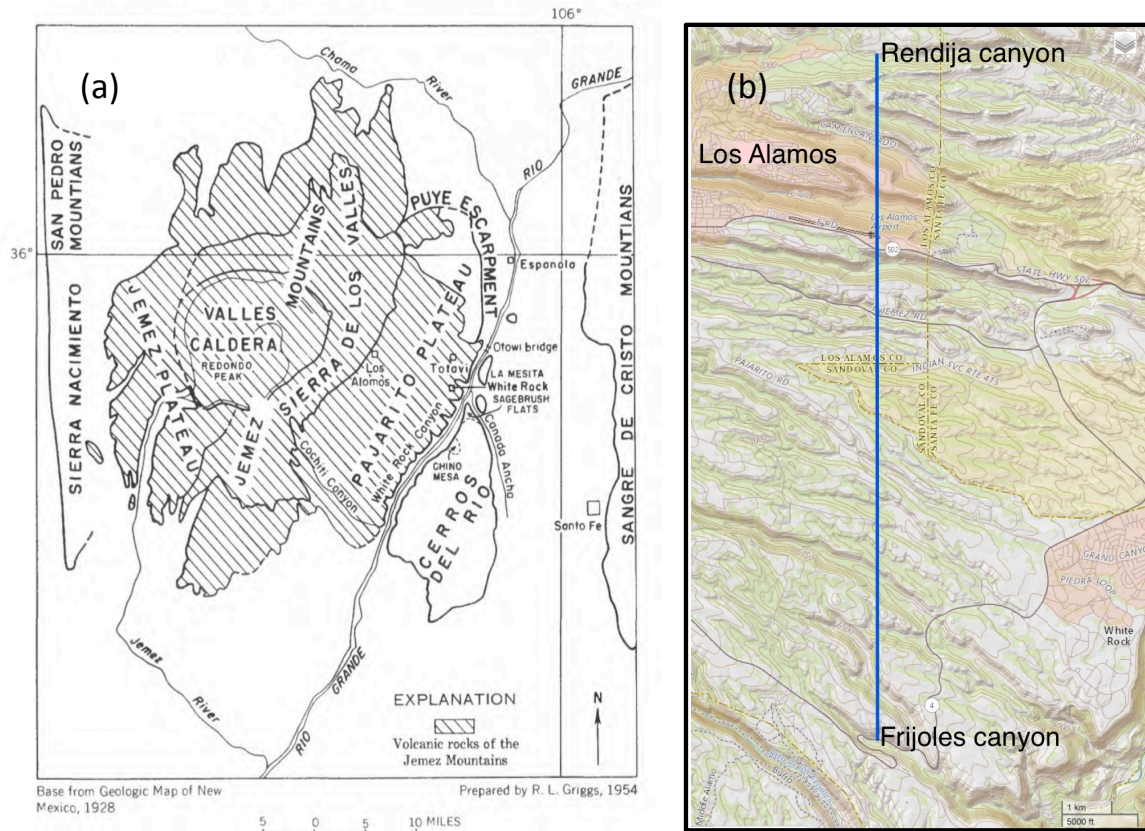


Figure 1. (a) Map showing topographic features in the Los Alamos region (reprinted from Griggs (1964)), and (b) topographic map of the region showing the variation in topography along the N-S 2D cross-section considered for this study (obtained from USGS digital elevation map).

10 m intervals is used for this study as the elevation profile does not change significantly from a sampling length of 1 m to that of 10 m. The overall elevation of the plateau changes by approximately 150 m over 12 km due to the change in proximity from the Caldera. The average slope of the mesas considered in this study is 20° with the slope varying between 10° and 26° .

The material in the different background layers for the HL and TL systems are assumed to be heterogeneous, linearly elastic with intrinsic attenuation, and each layer is taken to be horizontal. Thus, the velocity profile with depth is assumed to be the same along the entire cross-section. This velocity profile is chosen to be the same as that at the TA-55 LANL facility, obtained from fig. 4-3 of Wong et al. (2007). The detailed shear and P-wave velocity profile is shown in Fig. 3(a). From this figure, it can be seen that the shear wave velocity varies from 240 m/s at the free surface to 975 m/s at a depth of 123 m. The density of the material at the TA-55

1
2
3
4
5
6
7
8
9
10
11
12
13
14
15
16
17
18 **Figure 2.** Change in elevation along the 2D cross-section as a function of distance from Frijoles canyon
19 (solid blue line). Notice the different horizontal and vertical scales. The dashed black line marks the
20 average elevation of this region, which is 2050 m above sea level.
21

22
23 143 site [Fig. 3(b)], is taken from fig. 4-7 of [Wong et al. \(2007\)](#), and it varies between 1600 and
24
25 144 1700 kg/m^3 with depth. For the H and T systems, the soil is assumed to be homogeneous and
26
27 145 linearly anelastic with properties same as that at TA-55 at a depth of 123 m, i.e., with a shear
28
29 146 wave velocity of 975 m/s, P wave velocity of 2073 m/s and a density of 1700 kg/m^3 .
30

31 147 We model the internal friction in the layers using Rayleigh damping. It has long been ob-
32
33 148 served that the internal friction in rock and soil material at low frequencies, say less than 1
34
35 149 Hz ([Liu et al. \(1976\)](#)), can be approximated as a frequency-independent quantity, but at higher
36
37 150 frequencies, the amount of damping in the system decreases with frequency (e.g., [Sipkin & Jor-](#)
38
39
40
41
42
43
44
45
46
47
48
49
50
51
52
53
54
55

56 **Figure 3.** (a) S and P wave velocities and (b) density at the LANL TA-55 site as a function of depth.
57 Data obtained from [Wong et al. \(2007\)](#).
58
59
60

1
2
3 dan (1979) and Raof et al. (1999)). Withers et al. (2015) modeled this frequency-dependent
4
5 damping as a constant up to a transition frequency (f_T), beyond which damping decreases as a
6
7 power law. In terms of the fraction of critical damping, ξ , this behavior can be written as,
8
9

$$\xi(f) = \begin{cases} \xi_0, & f < f_T \\ \xi_0 \left(\frac{f_T}{f}\right)^\gamma, & f \geq f_T \end{cases} \quad (1)$$

10
11
12
13
14
15 In the present study, we adopt this model and choose a transition frequency of 1 Hz and
16
17 $\gamma = 0.8$ for the soil and rock material in the Los Alamos region. For this study, we approximate
18
19 Eq. 1 using Rayleigh damping. To select the appropriate coefficients α and β , which are the
20
21 multipliers for the mass and stiffness proportional terms of a viscously-damped system, we
22
23 make use of the corresponding damping ratio vs frequency relationship for Rayleigh damping.
24
25
26

$$\frac{\xi_R(f)}{\xi_0} = \alpha \frac{f_0}{2f} + \beta \frac{f}{2f_0} \quad (2)$$

27
28
29 in which ξ_0 and f_0 are a reference damping ratio, and a reference frequency, respectively.
30
31 Then, following the procedure in Bielak et al. (2011) for evaluating α and β , we use a least
32
33 squares approach to minimize the difference between $\xi_R(f)$ and the target damping $\xi(f)$ in
34
35 Eq. 1:
36
37
38
39

$$\min_{\alpha, \beta} \int_0^{f_{max}} [\xi_R(f) - \xi(f)]^2 df \quad (3)$$

40
41
42
43 Besides being frequency dependent, the intrinsic attenuation of the material depends, most
44
45 importantly, on its stiffness: the softer the material, the higher the damping ratio. This de-
46
47 pendence can be represented approximately as an inverse function of the shear wave velocity
48
49 (Olsen et al. (2003)). Here, we choose, specifically $\xi_0 = 5/V_s$, (shear wave velocity V_s in m/s);
50
51 substitution of this ξ_0 into Eq. 1 then defines completely the material damping model used in
52
53 this study.
54
55
56
57
58
59
60

2.2 Seismic sources

The LANL area is surrounded by a complex fault system called the Pajarito fault system with the Pajarito fault to the south and west, Rendija canyon fault to the east, Guaje mountain fault and Sawyer Canyon fault to the northeast and Santa Clara canyon fault to the north [fig. 5-4 of Wong et al. (2007)]. While the Pajarito and the Santa Clara canyon faults have a dip between 45° to 75° , the other three faults are steeper, with a dip between 60° to 90° [fig. 5-5 of Wong et al. (2007)]. Although earthquake activity in New Mexico since 1869 has been infrequent and low ($M < 6$), the presence of these Quaternary faults indicates that larger earthquakes with longer return periods might be possible in this region. Due to the presence of critical facilities at the LANL, such potential earthquakes need to be considered in seismic studies. Understanding the extent to which the topography of this region might alter the ground motion during such earthquakes becomes important.

For the current study, we first consider three point sources with a dip of 65° placed at 3 km, 6 km and 9 km, and 2 km below the free surface as shown in Fig. 4(a) to understand the effect of topography under simple seismic sources. Next, we consider a N-S oriented fault with 3 different dip angles - 0° , 45° and 65° - as shown in Fig. 4(b). The 0° (red) and 45° (blue) dip faults start at 5 km and end at 8 km while the 65° dip (purple) fault starts at 5.5 km and ends at 7.5 km. All three faults intersect at 6 km from Frijoles Canyon and 2 km below the ground surface. While a fault with 0° dip is unrealistic, this scenario is considered to compare with the current state of practice in design of nuclear power plants, where vertically propagating seismic waves are widely used. The faults are modeled as a linear superposition of 501-point sources, designed to produce a prescribed slip displacement along the fault. The moment magnitude of the earthquake generated when these faults rupture is directly proportional to the area of the fault rupture, the shear modulus of the homogeneous basement rock, and the induced slip (Aki & Richards (2012)). So, as long as the area of fault rupture and the total slip are the same for all rupture scenarios, as they are in this study, they produce exactly the same earthquake magnitude, irrespective of the dip angle of the fault, or the sequence in which the point sources are activated. However, as is well known, earthquakes of the same magnitude can produce

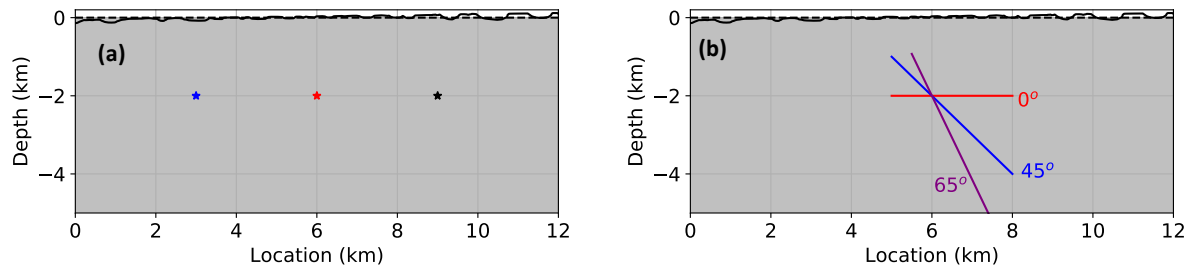


Figure 4. Sketch of a part of 12 km x 10 km 2D soil domain with (a) point sources located at 3 km, 6 km and 9km, and 2 km below the free surface, and (b) finite earthquake faults with dips of 0°, 45° and 65°.

widely different ground motions, depending on the depth of the hypocenter, dip, distance to the observation point, fault rupture sequence and spatial variability of slip along the fault.

To account for some of these variability in ground motion due to earthquake source parameters, we simulate two different types of earthquake fault ruptures - synchronous, where the entire length of the fault ruptures simultaneously to simulate approximately plane wave excitation in the central part of the fault at different angles of incidence, and asynchronous, where the rupture initiates at the hypocenter and propagates towards the ends of the fault with a prescribed constant propagation speed. When modeling the synchronous rupture, all 501-point sources are triggered simultaneously along the fault with a rake angle of 90°. This results in a normal fault rupture with the soil above the fault moving up and the soil below moving down. For the asynchronous rupture, the hypocenter is located at the point where the different faults intersect, i.e., 6 km along the 2D domain and 2 km below the free surface. The rupture then propagates to either side of the fault with a rupture speed of $0.8 V_s$ (- 780 m/s).

First, a uniform spatial slip distribution is assumed along the faults, i.e., the slip is assumed to vary only with time. The slip time function is similar to that used by [Imperatorii & Mai \(2015\)](#), which is a smoothed version of the Brune function ([Brune \(1970\)](#)) with three continuous derivatives at $t = 0$:

$$s(\omega, t) = \begin{cases} 0, & t < 0 \\ 1 - e^{-\omega t} \left[1 + \omega t + \frac{1}{2}(\omega t)^2 + \frac{1}{6}(\omega t)^3 - \left(\frac{3}{2x_o^2} + \frac{1}{3x_o} \right) (\omega t)^4 + \left(\frac{1}{x_o^3} + \frac{1}{6x_o^2} \right) (\omega t)^5 \right], & 0 \leq \omega t \leq x_o \\ 1 - e^{-\omega t} (1 + \omega t), & \omega t > x_o \end{cases} \quad (4)$$

where $x_o = 2.31$. The parameter ω in the above equation is chosen such that the corner frequency is 6.5 Hz. This choice of corner frequency ensures that ground motion with frequencies up to 10 Hz have noticeable contributions. The slip and the first three derivatives of the slip as a function of time as well as the Fourier transform of the slip velocity is presented in Fig. 1 of the electronic supplement. While this slip can be linearly scaled to achieve the desired earthquake magnitude, which is a function of the seismic moment $M_o = \text{shear modulus} * \text{area of fault rupture} * \text{total slip}$, we are mainly interested in the amplification caused due to topography in this study, which is independent of the actual magnitude of the earthquake due to the linear behavior of the soil.

To explore the effect of spatial variability of slip, three different random spatial factors ($g(x)$) are used to scale the slip time function $s(\omega, t)$ for the 65° dip fault. These randomized spatial factors are obtained such that their sum over the 501 point sources, i.e., $\sum_{i=1}^{501} g(x_i)$, is the same as that obtained in the uniform spatial slip scenario. This ensures that all these randomized slip scenarios result in the same magnitude of earthquake as the uniform slip scenario. The maximum slip as a function of location along the fault is presented in Fig. 5 for the four different spatial slip distributions considered in this study. A list of the various sources considered is tabulated in Table. 1.

2.3 2D finite element models and computational tool

To perform numerical simulations, we utilize the Multi-hazard Analysis for STOchastic time-DOMain phenomena (MASTODON) software framework (Coleman et al. (2017)) developed at the Idaho National Laboratory. This is an open source finite element tool, implicit in time, for solving nonlinear site-response and soil-structure interaction problems. These capabilities, which also entail wave propagation modeling, have been verified by Baltaji et al. (2017). Var-

1
2
3
4
5
6
7
8
9
10
11
12
13
14
15
16
17
18
19
20
21
22
23 **Figure 5.** Uniform slip and three different randomized maximum slips as a function of location along
24 the 65° fault. The sum of these slips is the same in all four cases.

25
26
27 ious short numerical verification examples that test various capabilities such as the time inte-
28
29 gration schemes, material models or the non-reflecting boundary conditions are available in the
30
31 tests directory on <http://github.com/idaholab/mastodon>.
32

33 The 2D finite element models considered for this study are 12 km wide and 10 km deep.
34
35 The actual domain is infinite in the horizontal and downward directions. In every case, the
36
37 causative fault is placed far enough from the left, right and bottom boundaries (by at least 2.5
38
39 km) of the computational domain to limit the occurrence of spurious wave reflections from
40
41 these truncating boundaries. Lysmer dampers (Lysmer & Kuhlemeyer (1969)) are placed at
42
43 these boundaries. Although Lysmer dampers do not completely absorb incident waves that are
44
45 not normal to the respective boundary, any residual waves that are reflected off the boundary
46
47 are likely small and greatly reduced by Rayleigh damping before they reach the mesa locations
48
49 on the top of the soil domain.
50

51 For the finite element simulations, the mesh size and the time step need to be sufficiently
52
53 small to accurately capture the wavelengths of the propagating waves up to the maximum fre-
54
55 quency of interest. Since MASTODON uses a stable implicit method of step-by-step integra-
56
57 tion, the calculations are unconditionally stable. The time step used for our calculations is 0.01
58
59 s, i.e., one tenth of the smallest period of interest. Similarly, the mesh size is chosen such that it
60

Table 1. List of earthquake sources simulated in this study. All four systems - flat-homogeneous half-space (H), homogeneous soil with mesas and canyons (T), flat-layered halfspace (HL), and layered halfspace with mesas and canyons (TL) are simulated under each of these source configurations.

Single point source			
Dip	Source location		
65°	x = 3 km, depth = - 2 km		
65°	x = 6 km, depth = - 2 km		
65°	x = 9 km, depth = - 2 km		
Finite fault			
Dip	Rupture type	Hypocenter	Spatial slip
0°	synchronous	-	uniform
45°	synchronous	-	uniform
65°	synchronous	-	uniform
0°	asynchronous	x = 6 km, depth = - 2 km	uniform
45°	asynchronous	x = 6 km, depth = - 2 km	uniform
65°	asynchronous	x = 6 km, depth = - 2 km	uniform
65°	asynchronous	x = 6 km, depth = - 2 km	Slip 1
65°	asynchronous	x = 6 km, depth = - 2 km	Slip 2
65°	asynchronous	x = 6 km, depth = - 2 km	Slip 3

is less than one fifth of the shortest wavelength for the 8-node serendipity elements (QUAD8) used in this study. Since this shortest wavelength is proportional to the shear wave velocity and inversely proportional to the maximum frequency, the maximum element size is different for each soil layer. In order to optimally mesh the 2D profile, the automatic mesher in MASTODON is used, which calculates and applies the maximum allowable mesh size for each soil layer. An octree-based approach is used to transition from the element size in one layer to the next.

3 RESULTS

As mentioned earlier, 36 different types of analyses were conducted using the 12 different types of earthquake sources presented in Table 1 on four different soil layering-topography configurations. The results from point sources simulations are discussed first followed by those from the finite fault ruptures.

3.1 Point sources:

To get a qualitative understanding of the differences in the response of the four computational models with/without soil layers and with/without surface topography, the horizontal (left column) and vertical velocities (right column) as a function of location at different time instants in all four systems are plotted in Fig. 6 for the point source located at 6 km. Comparisons between the velocities in the homogeneous halfspace (H - black curves) and that in the homogeneous soil with mesas and canyons (T - red curves) are presented in the top row, while comparisons between the layered halfspace (HL - black curves) and the layered soil with mesas and canyons (TL - red curves) are presented in the bottom row. The horizontal velocity in the homogeneous halfspace (H) shows the propagation of a well defined S wavefront. Comparing the two homogeneous soil domains (H and T) shows that addition of surface topography to the homogeneous halfspace causes scattered wavefronts, especially after the arrival of the main S wavefront. Topography also leads to significant backscattering of waves towards the source. However, the amplitudes of these scattered waves decay quite fast and the region above the source (6 km) becomes relatively silent ~ 5 s into the earthquake.

In the flat-layered halfspace (HL) scenario, in addition to the amplification of the S wave due to the trapping of waves in the layers, a significant part of the energy is also carried by large amplitude slow traveling surface waves farther away from the source, both of which lead to an increase of the duration of the earthquake. When surface topography is added on top of the layered halfspace (TL), the wave pattern becomes very complex and there is significant backscattering and trapping of waves due to both the topography as well as the soil layering. These results show that site specific soil-layering plays an important role in amplifying the effect of topography. So, through the rest of this paper, the HL scenario is used as the baseline

1
2
3
4
5
6
7
8
9
10
11
12
13
14
15
16
17
18
19
20
21
22
23
24
25
26
27 **Figure 6.** Horizontal (left column) and vertical (right column) velocities as a function of location at
28 different time instants for the point source located at 6 km. The black and red curves in the top row
29 correspond, respectively, to velocities in the homogeneous halfspace (H) and the homogeneous soil with
30 mesas and canyons (T), and those in the bottom figure correspond to velocities in the layered halfspace
31 (HL) and the layered soil with mesas and canyons (TL), respectively.
32
33
34

35
36 289 scenario against which the TL scenario would be compared to further understand the effect of
37 290 topography. These observations from Fig. 6 also agree well with those obtained by [Imperatori &](#)
38 291 [Mai \(2015\)](#) from their study on the effect of surface topography from the Swiss alpine regions.
39

40
41 292 To assess the overall effect of topography as a function of location along the mesas and
42 293 canyons, it is useful to introduce a metric that synthesizes the information in Figs. 6 into a
43 294 single number for each location and provides a measure of the intensity of the ground motion.
44 295 One such metric is the Housner Spectrum Index (HSI), defined in [Housner & Jennings \(1982\)](#)
45 296 as the integral of the velocity response spectrum over the frequency, 0.4 Hz to 10 Hz, for a
46 297 prescribed fraction of critical damping. Here, we will consider the velocity response spectrum
47 298 over the period interval, 0.4 Hz to 4 Hz to examine intermediate frequencies, for a critical
48 299 damping fraction of 0.05, and later introduce a modified version of this HSI, called MHSI,
49 300 in which, the spectral velocity is integrated between 3 Hz and 8 Hz in order to focus on the
50 301 higher-frequency components of the ground motion.
51
52
53
54
55
56
57
58
59
60

1
2
3
4
5
6
7
8
9
10
11
12
13
14
15
16
17
18
19
20
21
22
23
24
25
26
27
28
29
30
31
32
33 **Figure 7.** (a) Horizontal and vertical HSI for HL and TL for point source located at 6 km. Horizontal
34 and vertical HSI ratio (b) and MHSI ratio (c) calculated as the ratio of HSI or MHSI of TL to that of HL.

35
36
37 302 Fig. 7(a) shows the horizontal (X) and vertical (Y) HSIs both for the flat-layered halfspace
38 (dashed lines) and for the layered halfspace with surface topography (solid lines). From this
39 303
40 figure, we can make the following observations:
41 304

42
43 305 (i) The horizontal HSIs are, in general, significantly greater than the corresponding vertical
44 values, especially very close to the source.
45 306

46
47 307 (ii) For HL, the HSIs vary smoothly along the free surface. In comparison, for TL, each
48 HSI follows, generally, that for the corresponding flat-layered system, but exhibits significant
49 308
50 perturbations due to the mesas and canyons.
51 309

52
53 310 (iii) The largest perturbations tend to coincide with the locations where the changes in to-
54 pography are sharpest, corresponding to the steepest hills.
55 311

56
57 312 (iv) The surface topography gives rise to both amplification and deamplification of the HSI,
58 and at some sites, the changes occur rapidly over short distances.
59 313
60

1
2
3 314 (v) Farther away from the fault, the HSI decreases, and varies more slowly with location.
4
5

6 315 To quantify the degree of amplification or deamplification in the HSI due to the presence
7
8 316 of topography, Fig. 7(b) shows the HSI ratio as a function of location, calculated as the value
9
10 317 of HSI for the TL to that of the HL at the same location. It is noteworthy that the horizontal
11
12 318 HSI ratios have a similar shape as the topographic perturbations from the flat reference con-
13
14 319 figuration, with amplifications generally occurring in the mesas and deamplification or smaller
15
16 320 amplifications in the canyons. The resemblance, however, is stronger at some locations than at
17
18 321 others. The correlation is weaker in the vertical direction. The peak amplifications are on the
19
20 322 order of 3.7 in the horizontal and 2.8 in the vertical directions. By contrast, the strongest deam-
21
22 323 plification is about 0.34 in the horizontal direction, and with few exceptions (above 10 km),
23
24 324 there is no deamplification in the vertical direction.

25
26 325 The HSIs in Fig. 7(a) were calculated by integrating the spectral velocities between 0.4
27
28 326 and 4 Hz. These velocities are dominated by the contributions of the lower frequencies due
29
30 327 to the frequency content of the slip function. To examine the effects of topography at higher
31
32 328 frequencies (say, 3 to 8 Hz), we make use of a modified Housner Spectrum Intensity, MHSI,
33
34 329 which we calculate as the integral of the spectral velocity over frequency from 3 to 8 Hz.
35
36 330 Fig. 7(c) shows the MHSI ratio for the horizontal and vertical motions as a function of location.
37
38 331 This ratio is similar to the HSI ratio plotted in Fig. 7(b), but is calculated with the corresponding
39
40 332 MHSI values. One of the key differences between the MHSI ratios and the corresponding HSI
41
42 333 ratios is that the former are much noisier, that is, they vary much more rapidly with location
43
44 334 than the corresponding HSIs. On close observation we see that in the horizontal direction the
45
46 335 MHSI ratios are amplified and perturbed versions of the HSI ratios. The peaks in both sets of
47
48 336 ratios occur at around the same locations within the mesas, e.g., 2 km, 3.6 km, 3.8 km, and so
49
50 337 on, but the peaks of the MHSI tend to have higher amplification than those of HSI calculated
51
52 338 for lower frequencies, with a peak magnitude on the order of 6.4. However, deamplification is
53
54 339 also larger in MHSI, thus resulting in average amplifications of ~ 1.3 compared to no average
55
56 340 amplification/deamplification in the case of HSI. Similar to the horizontal direction, the peak
57
58 341 amplification observed from the MHSI ratio for the vertical motion (Fig. 7(c)) is much larger
59
60 342 than the vertical HSI ratio at similar locations. Amplification factors up to 4 are observed for the

1
2
3 343 MHSI(topo)/MHSI(flat) ratio for the vertical motion near the source. This strong local effect
4
5 344 at high frequencies can have practical implications for the design of safety-related nuclear
6
7 345 structures, both for structural systems, and particularly, for secondary systems.
8

9 346 **Detailed Spectral Velocity.** Both HSI and MHSI provide a measure of the spectral velocity
10
11 347 averaged over prescribed frequency ranges. They do not provide any information, however, on
12
13 348 the effect of topography at individual frequencies. For this purpose, it is useful to examine the
14
15 349 spectral velocity as a function of both frequency and location. Such spectra are shown in Fig. 8,
16
17 350 for the horizontal component of ground motion for the point source located at 6 km.

18
19 351 Results are shown in Fig. 8(b) for the flat-layered halfspace, and in Fig. 8(c) for the layered
20
21 352 halfspace with surface topography included. Both panels exhibit a frequency band centered
22
23 353 around 8 Hz near the source (~ 6.5 km), which exhibit peaks that might correspond to frequency
24
25 354 of the layered system (~ 7.7 Hz). To examine whether this is the case or whether the increase in
26
27 355 spectral values are associated with the source (and are generated independently of the layers),
28
29 356 we also show, in Fig. 8(a), the velocity spectra for the homogeneous halfspace. Interestingly,
30
31 357 the distinct frequency band visible in Figs. 8(b) and 8(c) does not appear in Fig. 8(a), which has
32
33 358 an almost uniform response in frequencies between 1 and 8 Hz near the source. This suggests
34
35 359 the amplification in response near 8 Hz in both HL and TL is due to the resonance of the soil
36
37 360 layers near this frequency at this location. In addition to these effects, Fig. 8(c) shows that
38
39 361 the mesas and canyons have a pronounced spatial scattering effect, which gives rise to a rapid
40
41 362 spatial variability of the spectral velocity with alternating amplifications and deamplifications,
42
43 363 in comparison to the smoothly varying spectra of the flat-layered halfspace.

44
45 364 This effect of topography can be clearly seen in Fig. 8(d), which shows the ratio of the
46
47 365 spectral velocities between TL and HL. This panel shows that the presence of canyons and
48
49 366 mesas leads to significant amplifications or deamplifications, depending on spatial location and
50
51 367 frequency; but the pattern of these amplifications or deamplifications is not readily predictable.
52
53 368 For instance, whereas the mesa around 9.5 km experiences a deamplification between 0.3 and
54
55 369 0.5 at frequencies below 2 Hz, the same mesa experiences amplifications greater than 2 at many
56
57 370 frequencies above 4 Hz.

58
59 371 **Effect of source location.** To understand the extent to which the effect of topography is af-

1
2
3
4
5
6
7
8
9
10
11
12
13
14
15
16
17
18
19
20
21
22
23
24
25
26
27
28
29
30
31
32
33
34
35
36
37
38
39
40
41
42
43
44
45
46
47
48
49
50
51
52
53
54
55
56
57
58
59
60

Figure 8. Horizontal spectral velocity as a function of frequency and location along the free surface for (a) homogeneous halfspace (H), (b) flat-layered halfspace (HL) and (c) layered halfspace with surface topography (TL) subjected to point source at 6 km. (d) Spectral ratio calculated as spectral velocity in TL to that in HL.

1
2
3
4
5
6
7
8
9
10
11
12
13
14
15
16
17
18
19
20
21
22
23
24
25
26
27
28
29
30
31
32 **Figure 9.** Horizontal and vertical HSIs for HL and TL as a function of location for point sources located
33 at 3 km, 6 km and 9 km.
34

35
36 372 affected by the proximity to the source, the response of the four systems were simulated under the
37
38 373 three different point source locations listed in Table 1. Fig. 9 presents the horizontal and vertical
39
40 374 HSI for the HL and TL scenarios as a function of location for all three sources. As expected,
41
42 375 in the HL scenario that has a flat free-surface (dashed lines), the HSIs for the 3 sources are
43
44 376 identical with respect to the source location. While the horizontal HSIs in the TL scenarios are
45
46 377 perturbed versions of those from the corresponding HL scenarios, there are subtle differences
47
48 378 in the amplitudes and form of these perturbations for the three cases as these perturbations are
49
50 379 correlated with the surface topography at each of these location. Although the vertical HSIs do
51
52 380 not follow the topography, these HSIs do vary significantly with the source location in the TL
53
54 381 scenario.

55
56 382 Fig. 10 presents the HSI ratios, calculated as the HSI for the TL scenario divided by the HL
57
58 383 scenario, as a function of location for the three point sources. The HSI ratios in both the horizon-
59
60 384 tal and vertical directions peak near the source indicating that the amplification caused within

1
2
3
4
5
6
7
8
9
10
11
12
13
14
15
16
17
18
19
20 **Figure 10.** Horizontal (top) and vertical (bottom) HSI ratios (TL/HL) as a function of location for point
21 sources located at 3 km, 6 km and 9 km.

22
23
24 385 2 km of the point source is due to a combination of source characteristics and topographic ef-
25
26 386 fects. However, farther away from the source, the horizontal HSI ratios are less affected by the
27
28 387 source as evidenced by almost identical X HSI ratios above 8 km for the sources at 3 km and
29
30 388 6 km (green and black lines), and also below 4 km for the sources at 6 km and 9 km (green
31
32 389 and brown lines). Unlike in the horizontal direction, the vertical HSI ratios look quite different
33
34 390 even at distances greater than 2 km from the source.

391 **3.2 Finite fault ruptures:**

392 The previous subsection detailed the effect of topography under the effect of a single point
393 source placed at different locations along the model. However, earthquake fault ruptures are
394 more complex than the rupture of single point sources. In this section results from the finite fault
395 rupture scenarios described in Table 1 are discussed. To understand the differences between the
396 synchronous and asynchronous fault rupture scenarios, snapshots of the response of the region
397 of interest in the TL model to synchronous and asynchronous fault rupture resulting from a
398 fault with a 65° dip is presented in Fig. 11.

399 In the synchronous scenario (left column), all the 501-point sources are triggered at the
400 same time. As expected, the generated wave front is similar to an inclined plane wave, with the
401 exception of the two circular wave fronts generated at the ends of the fault. The path taken by

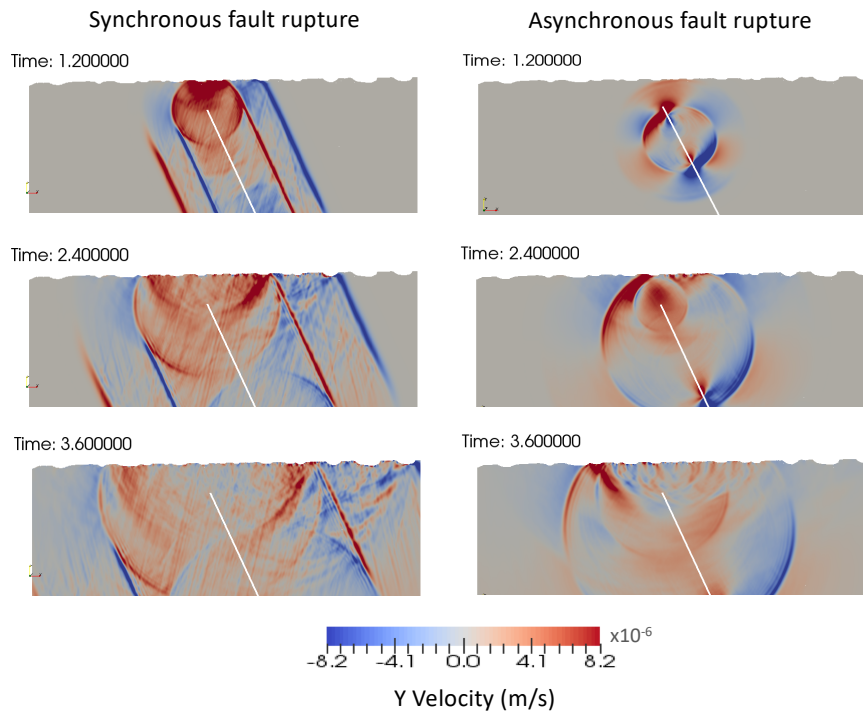


Figure 11. Snapshots of wave pattern resulting from synchronous (left column) and asynchronous (right column) fault ruptures in the layered halfspace with surface topography. The white line in these images represents the fault with 65° dip angle and the contours represent the vertical velocity.

the initial wave front as it traverses the soil domain, as well as those taken by the reflected and scattered waves generated from the interaction of this initial wave front with the free surface, can be seen in these snapshots. Disturbance of the wave pattern near the free surface caused by the presence of the surface topography, and to a smaller extent by the soil layers with varying shear wave velocities, can also be observed in these snapshots. In particular in the snapshot at 3.6 s for the synchronous scenario, the free surface located above the tip of the fault continues to vibrate long after the majority of the incoming seismic waves have traveled past this point indicating the presence of backscattered waves similar to those observed in Fig. 6.

In the asynchronous case (right column), the fault rupture nucleates at the hypocenter (located at 6 km and at a depth of -2 km), and then propagates up and down the fault with a constant rupture velocity, as opposed to all regions of the fault rupturing simultaneously as in

1
2
3 413 the synchronous fault rupture scenario. The resulting waves are very different from the inclined
4
5 414 plane waves in synchronous scenario. However, the scattering of waves and the elongation of
6
7 415 the ground motion duration due to the presence of topography observed in the synchronous
8
9 416 scenario are also visible in the asynchronous scenario. Another important observation regard-
10
11 417 ing the asynchronous fault rupture is that the maximum impact of the earthquake occurs close
12
13 418 to where the extension of the fault intersects the free surface, both on the hanging and on the
14
15 419 foot walls. This location of maximum amplitude in inclined propagating fault ruptures agrees
16
17 420 with previously reported results by [Boore & Zoback \(1974\)](#). By contrast, the maximum free
18
19 421 surface response in the synchronous wave rupture scenarios occurs at the location where the
20
21 422 inclined wave front meets the free surface. These observations are also confirmed in the hor-
22
23 423 izontal and vertical velocities plotted as a function of location at various time instants for the
24
25 424 asynchronous and synchronous 65° fault dip (Fig. 2 of electronic supplement). Through the rest
26
27 425 of this subsection, we will consider only the asynchronous fault rupture scenarios as they are
28
29 426 more realistic than the synchronous, pseudo plane-wave simulations.

31
32 427 ***Effect of fault dip:*** To understand the effect of fault dip on the topographic response of the
33
34 428 models, Fig. 12 shows the horizontal (X) HSI (red lines) and vertical (Y) HSI (black lines),
35
36 429 corresponding to the three dip angles considered (0° , 45° , and 65°), both for the flat-layered
37
38 430 halfspace (dashed lines) and for the layered halfspace with surface topography (solid lines) un-
39
40 431 der uniform spatial slip distribution along the fault in all three cases. As in the scenario with the
41
42 432 point source at 6 km (Fig. 7(a)), the HSI for the TL scenarios are perturbed versions of those
43
44 433 corresponding to the HL scenarios. For the dipping faults, the largest values of HSI generally
45
46 434 occur on the hanging wall, in the vicinity of the virtual intersection of the fault with the free
47
48 435 surface, similarly to where the maximum response occurs in the snapshots corresponding to
49
50 436 the asynchronous fault rupture in Fig. 11. As with the point sources, the HSI decreases and
51
52 437 varies more slowly with location farther away from the faults, which are located between 5 and
53
54 438 8 km. In particular, for the horizontal fault, the free surface ground motion is more similar in
55
56 439 the horizontal and vertical directions between 0 and 4 km, and also between 8 and 12 km, and
57
58 440 the topography effects are much smaller at these locations farther away from the fault than in
59
60 441 the region directly above the fault. For the dipping faults, the HSI is greater for the horizontal

1
2
3
4
5
6
7
8
9
10
11
12
13
14
15
16
17
18
19
20
21
22
23
24
25
26
27
28
29
30
31 **Figure 12.** Horizontal and vertical HSI for HL and TL as a function of location for the asynchronous
32 rupture of finite faults with dips of 0° , 45° and 65° . The slip has a uniform spatial distribution along the
33 length of the fault in all three cases.
34
35

36
37 442 than for the vertical motion, and the topography effects are more pronounced even farther away
38
39 443 from the fault.
40

41 444 Fig. 13 presents the horizontal and vertical HSI ratios calculated as the HSI for the TL
42
43 445 scenario to that of the HL scenario for all three fault dips. The horizontal HSI ratios for all three
44
45 446 fault dips look very similar between 8 and 12 km, and the HSI ratios for the two dipping faults
46
47 447 are identical between 0 and 5 km. The horizontal HSI ratio for the horizontal fault between 0
48
49 448 and 5 km follows a similar trend as the dipping faults, but with higher amplifications at most
50
51 449 of the locations. In the region close to the fault (between 5 and 8 km), there are differences
52
53 450 between the values of the ratios for the three cases, but even in these near fault regions, the
54
55 451 HSI ratios are well correlated with the surface topography. The peak horizontal ratios observed
56
57 452 here (~ 2.2) are much smaller than those observed in the scenarios with the point sources. In
58
59 453 the vertical direction, the HSI ratios from the three faults are very similar between 0 and 5 km
60

1
2
3
4
5
6
7
8
9
10
11
12
13
14
15
16
17
18
19
20 **Figure 13.** Horizontal (top) and vertical (bottom) HSI ratios (TL/HL) as a function of location for the
21 asynchronous rupture of finite faults with dips of 0° , 45° and 65° .

22
23
24 and also between 8 and 12 km. However, these ratios are quite different directly above the fault.
25
26 These results agree well with the observations from the point source simulations in that, farther
27
28 away from the fault, the source characteristics do not contribute significantly to the HSI ratios,
29
30 and the observed amplifications/deamplifications in HSI in these regions are mainly due to the
31
32 presence of surface topography.
33

34 *Effect of randomized spatial slip distribution:* The finite fault scenarios discussed previ-
35
36 ously assumed a uniform distribution of slip along the fault. In reality, the slip distribution along
37
38 the fault is quite heterogeneous and many researchers (e.g., [Somerville et al. \(1999\)](#) and [Mai
39 & Beroza \(2002\)](#)) have developed techniques to generate spatially heterogeneous slip distribu-
40
41 tions to fit certain wave number properties for finite planar faults. Since the fault considered in
42
43 this study is a line fault, we have randomized the spatial slip distribution, as described in Sec-
44
45 tion 2.2, such that the total slip from the event is the same as that in the uniform slip scenarios
46
47 (Fig. 5). The horizontal and vertical HSIs for the HL and TL scenarios for the finite fault with a
48
49 dip of 65° under the four different slip distributions are presented in Fig. 14. The vertical HSIs
50
51 for both the HL and TL scenarios look very similar across the different slip distributions. In the
52
53 horizontal direction, however, there are small differences in the magnitude of the peak HSIs,
54
55 but the overall shape of the HSIs are very similar across all four slip distributions.
56
57

58 The horizontal and vertical HSI ratios, calculated as the HSI for the TL to that of HL
59
60

1
2
3
4
5
6
7
8
9
10
11
12
13
14
15
16
17
18
19
20
21
22
23
24
25
26
27
28
29
30
31 **Figure 14.** Horizontal and vertical HSI for HL and TL as a function of location for the asynchronous
32 rupture of a finite fault with a 65° dip under four different spatial slip distributions.

33
34
35 472 scenario, for the four slip distributions are presented in Fig. 15. The HSI ratios in both the
36
37 473 horizontal and vertical directions are almost identical between 0 and 6 km across all four sce-
38
39 474 narios. Between 6 and 12 km, the ratios are very similar to each other, following the same
40
41 475 trend, but with slightly different amplification factors. These results suggest that the spatial slip
42
43 476 distributions do not significantly affect the topographic amplification factors at a location.
44
45
46

47 477 **3.3 Comparisons with ambient vibration studies:**

48
49 478 In the experiment conducted by [Stolte et al. \(2017\)](#), a 50 m tall and 185 m wide ridge was in-
50
51 479 strumented with stations located at the foot of the ridge, along the slope, top of the ridge, and a
52
53 480 station located in the canyon relatively far from the ridge that could serve as a reference ground
54
55 481 motion that is unaffected by the presence of the ridge. While the mesas modeled in this numer-
56
57 482 ical study are not of the same dimensions as the instrumented mesa, the fundamental frequency
58
59 483 of one of the mesas located between 7.33 and 7.92 km, calculated using the approximate analyt-
60

1
2
3
4
5
6
7
8
9
10
11
12
13
14
15
16
17
18
19
20 **Figure 15.** Horizontal (top) and vertical (bottom) HSI ratios (TL/HL) as a function of location for the
21 asynchronous rupture of a finite fault with a 65° dip under four different spatial slip distributions.
22

23
24 484 ical expression derived by Paolucci (2002), is around 2.18 Hz, and this frequency is close to that
25
26 485 of the instrumented ridge (~ 1.5 Hz calculated using the same method). The Paolucci (2002)
27
28 486 expression estimates an upper bound on fundamental frequency of a 2D triangular topograph-
29
30 487 ical feature. While the expression was derived for 2D triangular features, Paolucci used the
31
32 488 same approximate expression to estimate the natural frequency of a mesa-like feature, Civita
33
34 489 di Bagnoregio located in Central Italy. The fundamental frequency estimate obtained from the
35
36 490 analytical expression agreed well with that obtained from 3D numerical analysis of this feature
37
38 491 subject to vertically propagating S wave. In the present study, this conservative upper bound on
39
40 492 fundamental frequency is obtained as the ratio of the shear wave velocity to the feature length.
41
42 493 The average shear wave velocity of the layered soil domain considered is estimated to be 1286
43
44 494 m/s from the horizontal time histories in Fig. 6 and the toe-to-toe feature lengths for the mesa
45
46 495 is computed from Fig. 16.

47
48 496 The bottom subplot of Fig. 16 presents the mesa located between 7.33 and 7.92 km. The
49
50 497 blue and red dashed lines represent the stations at the foot of the mesa and along the slope of the
51
52 498 mesa, respectively. The purple and teal lines represent the stations near the edge of the mesa
53
54 499 and near the center of the mesa, respectively. Since the field study only contains the layered
55
56 500 halfspace with surface topography, the numerical study is conducted in the same manner by
57
58 501 taking the average of the response at the two canyon stations (light brown) on the two sides
59
60

1
2
3
4
5
6
7
8
9
10
11
12
13
14
15
16
17
18
19
20
21
22
23
24
25
26
27
28 **Figure 16.** Median horizontal and vertical spectral velocity ratios at various locations on the mesa as a
29 function of a dimensionless frequency, normalized with respect to the estimated fundamental frequency
30 of the mesa (1.25 Hz). The average of the spectral velocities at the reference station on either side of the
31 mesa is used as the reference spectral velocity to compute the ratios. Spectral velocity ratios from 12
32 different source configurations and 2 stations each at the toe, slope, mesa-edge and top of the mesa are
33 used to compute the median spectral velocity ratios.
34
35
36
37

38
39 502 of the mesa as the reference ground motion. These two reference canyon stations are assumed
40 503 to be sufficiently far away from the mesa to be unaffected by the presence of this mesa or the
41 504 other neighboring topographical features. The horizontal (X) and vertical (Y) spectral velocity
42 505 ratios at different stations are then obtained by dividing the spectral velocities at the respective
43 506 stations by the reference spectral velocity. The spectral velocity ratios are computed for all 12
44 507 source configurations from Table. 1 for the two stations of each type (toe, slope, mesa edge
45 508 and mesa). The median horizontal (X) and vertical (Y) spectral velocity ratios for each type of
46 509 station (from a sample set of 24) as a function of normalized frequency are presented in Fig. 16.
47 510 The frequencies are normalized by 1.25 Hz, which is the frequency of the mesa's first peak in
48 511 the transfer function for the amplitudes of the velocity spectrum at the center of the mesa to that
49 512 of the average of the corresponding values for the two reference stations within the neighboring
50
51
52
53
54
55
56
57
58
59
60

1
2
3 513 canyons. Note that this normalization frequency lies below 2.18 Hz, the analytical upper bound
4
5 514 obtained using the Paolucci triangular wedge approximation.
6

7 515 From the horizontal spectral velocity ratios in Fig. 16, the following observations can be
8
9 516 made:

10
11 517 (i) There are two main frequencies at which the X spectral ratio peaks - one is at 1.25 Hz,
12
13 518 with which the frequencies have been normalized, and the other occurs at about 3 Hz ($\sim 2.4x$
14
15 519 the fundamental frequency), which is likely a higher mode of the mesa.

16
17 520 (ii) Up to 3x the fundamental frequency of the mesa, the amplifications are the highest at
18
19 521 the stations located at the top of the mesa near the edge (purple lines), followed by the stations
20
21 522 located on the top of the mesas (teal lines) that have the second highest amplifications. In the
22
23 523 ambient vibration experiment, of the three stations considered on top of the mesa, two were
24
25 524 close to the edge of the mesa and one was farther away from the edge where the topography
26
27 525 was relatively flat. It was observed that the stations near the edge had slightly higher maximum
28
29 526 spectral ratio (five at stations near mesa-edge, compared to four farther away from the edge).

30
31 527 (iii) Up to 3x the fundamental frequency of the mesa, the stations located on the slope (red
32
33 528 dashed lines) and the toe (blue dashed lines) stations exhibit strong deamplification, beyond
34
35 529 which the toe stations have an amplified response. Also, the slope and toe stations have very
36
37 530 similar spectral ratios up to the fundamental frequency, beyond which the toe stations have a
38
39 531 higher spectral ratio than the stations on the slope. This is in contrast with the ambient vibration
40
41 532 experiments, where stations on the slope have a higher amplification ratio than the toe stations
42
43 533 near the fundamental frequency.

44
45 534 (iv) The median X spectral ratio for this mesa varies between 0.5 - 1.4. The maximum of
46
47 535 this median spectral ratio is much lower than that observed in the instrumented mesa, where
48
49 536 the stations at the top had maximum median amplifications up to 5. However, while the median
50
51 537 spectral ratios are relatively smaller for this mesa, maximum spectral ratios up to 5 are observed
52
53 538 for different source configurations (Fig. 17).

54
55
56
57 539 The median vertical (Y) spectral velocity ratios for this mesa show similar characteristics
58
59 540 as the horizontal response, with the spectral velocity at the stations near the edge of the mesa
60

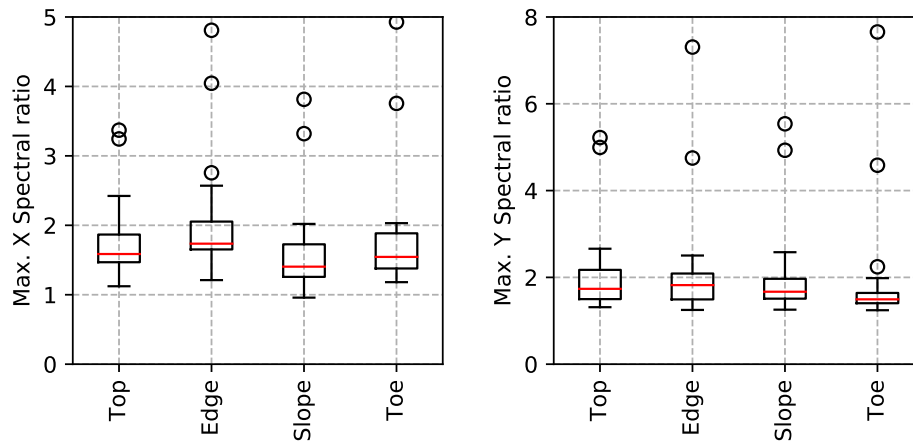


Figure 17. Box whisker plot presenting the maximum spectral ratio for different types of stations on the mesa for the various source configurations. The red line represents the median and the box extends from the first quartile (Q_1) to the third quartile (Q_3), i.e., the box encloses the center 50% of the data and of the remaining 50%, 25% are distributed below the lower end of the box, and the rest 25% are distributed above the upper end of the box. The lower end of the whiskers is located at the maximum of the smallest data point and $Q_1 - 1.5 \text{ IQR}$, where $\text{IQR} = Q_3 - Q_1$. Similarly, the upper end of the whiskers is located the minimum of the largest data point and $Q_3 + 1.5 \text{ IQR}$. The circles indicate the outliers that are not included between the whiskers.

(purple lines) exhibiting highest amplification, followed by the stations near the center on top of the mesa (teal purples), followed by the toe and slope stations. However, in the instrumented mesa in the vertical direction, the amplifications were highest at the stations near the center of the mesa, followed by the edge stations, and then the slope stations, and finally the toe stations. Similar trends were observed for another mesa in the present study located between 4.65 and 5.3 km (Figure 3 of the electronic supplement). The spread of the maximum spectral velocity at different stations over the sample set is presented in Fig. 17. This plot shows that the maximum spectral velocity ratio is about 5 in the X direction and 8 in the vertical direction, which are much closer to the maximum spectral velocity ratios of 10 observed in the ambient vibration experiment.

Overall, the spectral ratios from the ambient vibration experiment qualitatively agree well with those observed in the mesa considered in this study near the fundamental frequency of the feature with the stations on top of the mesa experiencing higher response compared to slope and toe stations. The largest response was centered near the fundamental frequency in the

1
2
3 555 ambient vibration experiments. Thus, it is possible that the ambient vibrations did not excite
4
5 556 higher natural frequencies. However, since the ground motion used in this study had energy
6
7 557 in a wider frequency range, amplification was observed at multiple frequencies between 1-10
8
9 558 Hz. It is possible that some of those frequencies correspond to the higher natural vibration
10
11 559 modes of the feature. Finally, the differences in the response of the mesas may be attributed to
12
13 560 the differences in the geometry of the mesa as well as the neighboring topographical features
14
15 561 between the ambient vibration experiment and this computational study, as well as the relatively
16
17 562 close proximity of the chosen mesas to the earthquake sources considered.
18
19
20

21 563 **4 DISCUSSION AND CONCLUSIONS**

22
23
24 564 In this study, we analyzed the responses of mesas and canyons atop a layered halfspace, which
25
26 565 is representative of the topography in the Los Alamos area, under earthquake waves generated
27
28 566 from both point sources and inclined faults with three different dips, - 0° , 45° and 65° . Four
29
30 567 different systems are tested - a homogeneous halfspace, homogeneous halfspace with surface
31
32 568 topography, a flat-layered halfspace, and a layered halfspace with surface topography, to com-
33
34 569 pare ground response with and without surface topography in the presence or absence of soil
35
36 570 layers. These four systems were analyzed under the source configurations listed in Table 1 to
37
38 571 explore the sensitivity of the results to various source characteristics such as source location,
39
40 572 synchronous vs asynchronous rupture of finite faults with varying dips, as well as uniform vs
41
42 573 randomized spatial distribution of slip along the finite faults.
43

44 574 Velocity seismograms as a function of location at different time instants from the two ho-
45
46 575 mogeneous systems with/without surface topography show that the presence of topography
47
48 576 causes waves to backscatter towards the source, but these scattered waves decay relatively fast
49
50 577 in the homogeneous soil domain. The addition of soil layers creates a variation of shear wave
51
52 578 velocity with depth, and this amplifies the soil response near the fundamental frequency of the
53
54 579 layers and also generates large amplitude surface waves. When surface topography is added to
55
56 580 the layered soil domain, there is significant backscattering and trapping of waves due to both
57
58 581 surface topography as well as the soil layers. Note that while the effect of depth varying shear
59
60 582 wave velocity is considered in this study, finer soil heterogeneities that could result in a ran-

1
2
3 583 domized spatial shear wave velocity distribution are not considered in this study. [Imperator](#)
4
5 584 & [Mai \(2015\)](#) showed that finer soil heterogeneities in a halfspace without surface topography
6
7 585 cause similar scattering of seismic waves to that caused by surface topography. However, the
8
9 586 combined effect of finer soil heterogeneities along with surface topography is outside the scope
10
11 587 of this study.

12
13 588 Snapshots from the synchronous and asynchronous fault rupture scenarios show that the
14
15 589 wave fields generated by both types of rupture are quite different, and that the rupture type
16
17 590 and fault dip dictate the region of maximum impact along the free surface. While the peak
18
19 591 response occurs on the hanging wall for the synchronous rupture scenario, the major impact of
20
21 592 the earthquake is felt in a more localized region at the virtual intersection of the fault with the
22
23 593 free surface on both the hanging and foot wall in the asynchronous fault rupture scenario. Due
24
25 594 to these differences in location of peak response, the rupture type and the local fault geometry
26
27 595 play an important role in the placement of structures with respect to a known fault.

28
29 596 To quantify the effect of topography, the spectral velocity along the free surface is exam-
30
31 597 ined using multiple methods to understand both the global and local effects of topography.
32
33 598 The HSI, which is the integral of spectral velocity between 0.4 - 4 Hz, MHSI, which is the
34
35 599 integral of spectral velocity between 3 - 8 Hz, HSI ratio ($\text{HSI}(\text{topo})/\text{HSI}(\text{flat})$) and MHSI ratio
36
37 600 ($\text{MHSI}(\text{topo})/\text{MHSI}(\text{flat})$), are shown to be useful metrics to describe the overall response of the
38
39 601 free surface as a function of topography. The HSI and MHSI ratios in the horizontal direction
40
41 602 are well correlated with the perturbations of the terrain from the flat reference configuration for
42
43 603 all source configurations with amplifications at the mesas and deamplification or smaller ampli-
44
45 604 fication in the canyons. Also, higher amplification is observed at locations with steeper changes
46
47 605 in topography, and also at regions closer to the source. The correlation between topography and
48
49 606 the spectral response is much weaker in the vertical than in the horizontal direction. From the
50
51 607 HSI ratios for the cases with different point source locations (Fig. 10), fault dips (Fig. 13) and
52
53 608 spatial variations of slip along the fault (Fig. 15), it can be observed that the horizontal HSI
54
55 609 ratios farther away from the source are almost independent of the individual source character-
56
57 610 istics. The same is true for the vertical HSI ratios with variations in fault dip and spatial slip
58
59 611 distribution, but the vertical HSI ratios are more sensitive to the point source location than the

1
2
3 612 ratios in horizontal direction, even at distances more than 2 km from the point source. While
4
5 613 the HSI ratios close to the source are quite different when the point source location and fault dip
6
7 614 are varied, the ratios in both directions are not significantly affected by changes in the spatial
8
9 615 slip distribution along the fault.

10
11 616 To better understand the effect of mesas, a mesa with fundamental frequency similar to that
12
13 617 of the mesa instrumented by [Stolte et al. \(2017\)](#), was studied in detail by analyzing the me-
14
15 618 dian spectral velocity ratios at multiple locations in and around the mesa from all the different
16
17 619 source configurations. Average spectral velocity at the canyon stations located on either sides
18
19 620 of the mesa is used as the reference for calculating the spectral velocity ratios. In this study, the
20
21 621 stations located on top of the mesas exhibited larger response in both horizontal and vertical
22
23 622 directions compared to those located at the slope or near the foot of the mesa, near the fun-
24
25 623 damental frequency of the mesa. These observations are consistent with those made from the
26
27 624 ambient vibration experiments conducted by [Stolte et al. \(2017\)](#). Away from the fundamental
28
29 625 frequency, the same trend continued up to frequencies less than 3x the fundamental frequency.

30
31 626 While the maximum amplification due to topography as measured by the HSI ratios is
32
33 627 around 4 in both the horizontal and vertical directions, in most cases and locations, the HSI
34
35 628 ratios are much lower (between 0.34 and 2). A similar range (0.5 - 1.5) is observed in the
36
37 629 median spectral velocity ratios at individual frequencies along the mesa in Fig. 16. However,
38
39 630 the maximum spectral velocity ratios exhibit a much higher peak compared to the HSI ratios,
40
41 631 with values between 5 and 8 in the horizontal and vertical directions, respectively. These results
42
43 632 suggest that even these seemingly small topographical features with heights less than 100 m,
44
45 633 can alter the free surface response substantially at particular frequencies. The maximum ampli-
46
47 634 fication factors observed in this study are in the same range as those observed in the ambient
48
49 635 vibration study conducted by [Stolte et al. \(2017\)](#). These levels of amplification are much higher
50
51 636 than the safety factor of 1.2, suggested by [Eurocode-8 \(2000\)](#) to account for the effect of topog-
52
53 637 raphy due to the presence of features similar to the mesas considered in this study. It should be
54
55 638 noted, however, that the soil response is assumed to be linear anelastic, and the large amplifica-
56
57 639 tion ratios occur only at isolated frequencies. Considering nonlinear soil behavior could result
58
59 640 in smaller amplification factors when large soil strain levels are generated by the earthquake.

1
2
3
4
5
6
7
8
9
10
11
12
13
14
15
16
17
18
19
20
21
22
23
24
25
26
27
28
29
30
31
32
33
34
35
36
37
38
39
40
41
42
43
44
45
46
47
48
49
50
51
52
53
54
55
56
57
58
59
60

641 The results from this study suggest that the response at a site is inherently coupled with the
642 type of earthquake fault, rupture type, source characteristics, soil properties and topography.
643 However, dividing the response of the layered halfspace with surface topography by that of
644 the flat-layered halfspace reduces the sensitivity of the results to the source characteristics and
645 to the soil properties, and isolates the effects of topography to some extent, especially farther
646 away from the fault. Therefore, even though the particular input slip time history and constant
647 rupture velocity used in this study does not correspond to a specific earthquake source, based on
648 the results from this study, we expect the spectral ratios and HSI ratios to remain valid for other
649 slip functions and rupture velocity distributions, especially farther away from the fault. While
650 these ratios follow similar trends for different earthquake sources, the levels of amplification
651 closer to the fault are quite sensitive to the fault geometry and particular rupture mechanism,
652 indicating that the effect of fault geometry and topography cannot be completely decoupled.
653 This reinforces the conclusion from other studies that a site-specific analysis considering local
654 earthquake fault geometries, topography and soil stratigraphy at that location is important for
655 the design of critical infrastructure at that location.

656 ACKNOWLEDGMENTS

657 The authors would like to thank the Department of Energy's NNSA Nuclear Safety Research
658 and Development (NSR&D) program for providing the funding to support this research. The
659 authors would also like to thank Dr. Chandrakanth Bolisetti for his insightful comments on the
660 manuscript. They would also like to thank Prof. Martin Mai, and two anonymous reviewers for
661 their thoughtful review, which significantly helped improve the article.

662 REFERENCES

- 663 Aki, K. & Richards, P. G., 2012. *Quantitative Seismology*, University Science Books.
664 Anoshehpour, A. & Brune, J. N., 1989. Foam rubber modeling of topographic and dam interaction
665 effects at pacoima dam, *Bull. Seismol. Soc. Am.*, **79**(5), 1347–1360.
666 Ashford, S. A. & Sitar, N., 1997. Analysis of topographic amplification of inclined shear waves in a
667 steep coastal bluff, *Bull. Seismol. Soc. Am.*, **87**(3), 692700.

- 1
2
3 668 Assimaki, D. & Jeong, E., 2013. Ground-motion observations at hotel montana during the m 7.0 2010
4 Haiti earthquake: Topography or soil amplification, *Bull. Seismol. Soc. Am.*, **103**(5), 25772590.
5 669
6 670 Baltaji, O., Numanoglu, O., Veeraraghavan, S., Hashash, Y. M. A., Coleman, J. L., , & Bolisetti, C.,
7 2017. *Non-linear time domain site response and soil structure analysis for nuclear facilities us-*
8 671 *ing MOOSE*, Proc. 24th International Conference on Structural Mechanics in Reactor Technology
9 672 (SMiRT 24), Busan, South Korea, August 2017.
10 673
11 674 Bard, P. Y., 1982. Diffracted waves and displacement field over two-dimensional elevated topographies,
12 *Geophys. J. Int.*, **71**(3), 731760.
13 675
14 676 Bielak, J., Karaoglu, H., & Taborda, R., 2011. Memory-efficient displacement-based internal friction
15 for wave propagation simulation, *Geophysics*, **76**(6).
16 677
17 678 Boore, D. & Zoback, M. D., 1974. Two-dimensional kinematic fault modeling of the Pacoima Dam
18 strong-motion recordings of the February 9, 1971, San Fernando earthquake, *Bull. Seismol. Soc. Am.*,
19 **64**, 555–570.
20 679
21 680
22 681 Bouchon, M., 1973. Effect of topography on surface motion, *Bull. Seismol. Soc. Am.*, **63**(2), 615632.
23 682
24 683 Brune, J. N., 1970. Tectonic stress and the spectra of seismic shear waves from earthquakes, *J. Geophys.*
25 *Res.*, **75**(26), 4997–5009.
26 684
27 685 Caserta, A., Bellucci, F., Cultrera, G., Donati, S., Marra, F., Mele, G., Palombo, B., & Rovelli, A.,
28 2000. Study of site effects in the area of Nocera Umbra (Central Italy) during the 1997 Umbria-
29 Marche seismic sequence, *J. Seismol.*, **4**(4), 555565.
30 686
31 687 Celebi, M., 1987. Topographical and geological amplifications determined from strong motion and
32 aftershock records of the 3 March 1985 Chile earthquake, *Bull. Seismol. Soc. Am.*, **77**(4), 1147–1167.
33 688
34 689 Coleman, J., Slaughter, A., Veeraraghavan, S., Bolisetti, C., Numanoglu, O., Spears, R., Hoffman, W.,
35 & Kurt, E., 2017. *MASTODON theory manual*, Idaho National Laboratory.
36 690
37 691 Costantino, C. & Houston, T., 2005. Sensitivity studies to estimate potential 2-dimensional effects at
38 the CMRR site on design ground motions, *unpublished technical report*.
39 692
40 693 Davis, L. L. & West, R., 1973. Observed effects of topography on ground motion, *Bull. Seismol. Soc.*
41 *Am.*, **63**(1), 283298.
42 694
43 695 Eurocode-8, 2000. *(EC8) Design provisions for earthquake resistance of structures, Part 1-1: General*
44 *Rules-Seismic Actions and General Requirements for Structures*, prEN. 1998-5, Brussels.
45 696
46 697 Geli, L., Bard, P., & Jullien, B., 1988. The effect of topography on earthquake ground motion: A review
47 and new results, *Bull. Seismol. Soc. Am.*, **78**(1), 4263.
48 698
49 699 Graizer, V., 2009. Low-velocity zone and topography as a source of site amplification effect on Tarzana
50 hill, California, *Soil Dyn. Earthq. Engg.*, **29**(2), 324–332.
51 700
52 701 Griggs, R. L., 1964. Geology and groundwater resources of the Los Alamos area, New Mexico.
53 702
54 703 Housner, G. W. & Jennings, P. C., 1982. *Earthquake design criteria*, Earthquake Engineering Research
55 Institute.
56
57
58
59
60

- 1
2
3
4
5
6
7
8
9
10
11
12
13
14
15
16
17
18
19
20
21
22
23
24
25
26
27
28
29
30
31
32
33
34
35
36
37
38
39
40
41
42
43
44
45
46
47
48
49
50
51
52
53
54
55
56
57
58
59
60
- 704 Imperatori, W. & Mai, P., 2015. The role of topography and lateral velocity heterogeneities on near-
705 source scattering and ground-motion variability, *Geophys. J. Int.*, **202**, 2163–2181.
- 706 Imperatori, W. & Mai, P. M., 2013. Broad-band near-field ground motion simulations in 3-dimensional
707 scattering media, *Geophys. J. Int.*, **192**, 725–744.
- 708 Lee, S. J., Chan, Y. C., Komatitsch, D., Huang, B. S., & Tromp, J., 2009. Effects of realistic surface
709 topography on seismic ground motion in the Yangminshan region of Taiwan based upon the spectral-
710 element method and Lidar DTM, *Bull. Seismol. Soc. Am.*, **99**(2A), 681693.
- 711 Liu, H., Anderson, D., & Kanamori, H., 1976. Velocity dispersion due to inelasticity; implications for
712 seismology and mantle composition, *Geophys. J. Int.*, **46**, 41–48.
- 713 Lovati, S., Bakavoli, M., Massa, M., Ferretti, G., Pacor, F., Paolucci, R., Haghshenas, E., & Kamalian,
714 M., 2011. Estimation of topographical effects at Narni Ridge (central Italy): Comparison between
715 experimental results and numerical modelling, *Bull. Earthq. Eng.*, **9**(6), 19872005.
- 716 Lysmer, J. & Kuhlemeyer, R. L., 1969. Finite dynamic model for infinite media, *J. Eng. Mech.*, **95**(4),
717 859878.
- 718 Mai, P. M. & Beroza, G. C., 2002. A spatial random field model to characterize complexity in earth-
719 quake slip, *J. Geophys. Res.*, **107**(B11).
- 720 Marzorati, S., Ladina, C., Falcucci, E., Gori, S., Ameri, G., & Galadini, F., 2011. Site effects on the
721 rock: The case of Castelvechio Subequo (L'Aquila, central Italy, *Bull. Earthq. Eng.*, **9**(3), 841868.
- 722 Maufroy, E., Chaljub, E., Hollender, F., Bard, P. Y., Kristek, J., Moczo, P., Martin, F. D., Theodoulidis,
723 N., Manakou, M., Guyonnet-Benaize, C., Hollard, N., & Ptilakis, K., 2016. 3D numerical simulation
724 and ground motion prediction: Verification, validation and beyondlessons from the E2VP project,
725 *Soil Dyn. Earthq. Eng.*, **91**, 53–71.
- 726 Moczo, P., Bystrick, E., Kristek, J., Carcione, J. M., & Bouchon, M., 1997. Hybrid modeling of P-SV
727 seismic motion at inhomogeneous viscoelastic topographic structures, *Bull. Seismol. Soc. Am.*, **87**(5),
728 1305–1323.
- 729 Olsen, K. B., Day, S. M., & Bradley, C. R., 2003. Estimation of Q for long-period (>2 sec) waves in
730 the Los Angeles basin, *Bull. Seismol. Soc. Am.*, **93**(2), 627638.
- 731 Paolucci, R., 2002. Amplification of earthquake ground motion by steep topographic irregularities,
732 *Earthq. Eng. Struct. Dyn.*, **31**(10), 18311853.
- 733 Pedersen, H., Le Brun, B., Hatzfeld, D., Campillo, M., & Bard, P. Y., 1994. Ground-motion amplitude
734 across ridges, *Bull. Seismol. Soc. Am.*, **84**, 1786–1800.
- 735 Poursartip, B., Fathi, A., & Kallivokas, L. F., 2017. Seismic wave amplification by topographic fea-
736 tures: A parametric study, *Soil Dyn. Earthq. Eng.*, **92**, 503527.
- 737 Raof, M., Herrmann, R., & Malagnini, L., 1999. Attenuation and excitation of three-component
738 ground motion in southern California, *Bull. Seismol. Soc. Am.*, **89**, 888–902.
- 739 Restrepo, D., Bielak, J., Gmez, J., Jaramillo, J., & Serrano, R., 2016. Effects of realistic topography on

- 1
2
3 740 the ground motion of the Colombian Andes -A case study of the Aburr Valley, Antioquia, *Geophys.*
4 *J. Int.*, **204**, 1801–1816.
5 741
6 742 Sanchez-Sesma, F. J., Herrera, I., & Aviles, J., 1982. A boundary method for elastic wave diffrac-
7 tion: Application to scattering of SH waves by surface irregularities, *Bull. Seismol. Soc. Am.*, **72**(2),
8 743 473490.
9 744
10 745 Silva, W. J., 2005. *Evaluation of the potential for topographic effects at the proposed location of the*
11 *CMRR facility (TA-55)*.
12 746
13 747 Sipkin, S. & Jordan, T., 1979. Frequency dependence of QScS, *Bull. Seismol. Soc. Am.*, **69**, 1055
14 –1079.
15 748
16 749 Somerville, P., Irikura, K., Graves, R., Sawada, S., Wald, D. J., Abrahamson, N., Iwasaki, Y., Kagawa,
17 T., Smith, N., & Kowada, A., 1999. Characterizing crustal earthquake slip models for the prediction
18 of strong ground motion, *Seism. Res. Lett.*, **70**(1), 59–80.
19 750
20 751 Spudich, P., Hellweg, M., & Lee, H. K., 1996. Directional topographic site response at Tarzana ob-
21 served in aftershocks of the 1994 Northridge, California, earthquake: Implications for mainshock
22 motions, *Bull. Seismol. Soc. Am.*, **86**(1b), 193208.
23 752
24 753 Stewart, J. P. & Sholtis, S. E., 2005. Case study of strong ground motion variations across cut slope,
25 *Soil Dyn. Earthq. Eng.*, **25**(7/10), 539545.
26 754
27 755 Stewart, J. P., Kwok, A., Hashash, Y., Matasovic, N., Pyke, R., Wang, Z., & Yang, Z., 2008. *Bench-*
28 *marking of nonlinear geotechnical ground response analysis procedures*, PEER report 2008/04.
29 756
30 757 Stolte, A. C., Cox, B. R., & Lee, R. C., 2017. An experimental topographic amplification study at Los
31 Alamos National Laboratory using ambient vibrations, *Bull. Seismol. Soc. Am.*, **107**(3), 1386–1401.
32 758
33 759 Withers, K., Olsen, K. B., & Day, S. M., 2015. Memory-efficient simulation of frequency-dependent
34 Q, *Bull. Seismol. Soc. Am.*, **105**(6), 31293142.
35 760
36 761 Wong, I., Kelson, K., Olig, S., Kolbe, T., Hemphill-Haley, M., Bott, J., Green, R., Kanakari, H., Sawyer,
37 J., Silva, W., Stark, C., Haraden, C., Fenton, C., Unruh, J., Gardner, J., Reneau, S., & House, L., 1995.
38 *Seismic hazard evaluation of the Los Alamos National Laboratory*, unpublished final report prepared
39 for the Los Alamos National Laboratory and the U.S. Department of Energy, 3 volumes.
40 763
41 764 Wong, I., Silva, W., Olig, S., Dober, M., Gregor, N., Gardner, J., Lewis, C., Terra, F., Zachariasen, J.,
42 & K. Stokoe, e. a., 2007. *Update of the probabilistic seismic hazard analysis and development of*
43 *seismic design ground motions at the Los Alamos National Laboratory*, URS Corporation, 25 May
44 765
45 766
46 767
47 768
48 769
49 770
50 771
51
52
53
54
55
56
57
58
59
60

771 This paper has been produced using the Blackwell Scientific Publications GJI L^AT_EX2e class file.

Electronic supplement

Figure 1: Left figure presents the slip, slip velocity, slip acceleration and derivative of acceleration as a function of time, generated using Eq. 4. Right figure presents the Fourier transform of the slip velocity as a function of frequency. The corner frequency is set to 6.5 Hz.

1
2
3
4
5
6
7
8
9
10
11
12
13
14
15
16
17
18
19
20
21
22
23
24
25
26
27
28
29
30
31
32
33
34
35
36
37
38
39
40
41
42
43
44
45
46
47
48
49
50
51
52
53
54
55
56
57
58
59
60

Figure 2: Horizontal and vertical velocity time history as a function of location at different time instants for the 65° fault dip for the TL(red) and HL(black) scenarios. This figures shows that, in the synchronous scenario, the maximum ground response occurs to the right of the fault, where the inclined wavefront interacts with the free surface. However, in the asynchronous scenario, the maximum ground response occurs at the location where the extension of the fault would intersect the free-surface.

1
2
3
4
5
6
7
8
9
10
11
12
13
14
15
16
17
18
19
20
21
22
23
24
25
26
27
28
29
30
31
32
33
34
35
36
37
38
39
40
41
42
43
44
45
46
47
48
49
50
51
52
53
54
55
56
57
58
59
60

Figure 3: Median horizontal and vertical spectral velocity ratios at various locations on the mesa as a function of a dimensionless frequency, normalized with respect to the estimated fundamental frequency of the mesa (0.8 Hz). The average of the spectral velocities at the reference station on either side of the mesa is used as the reference spectral velocity to compute the ratios. Spectral velocity ratios from 12 different source configurations and 2 stations each at the toe, slope, mesa-edge and top of the mesa are used to compute the median spectral velocity ratios. These results agree well the results presented for the mesa considered in the main manuscript and also with the results from Stolte et al. (2017).